Phonon dispersion and Raman scattering in hexagonal GaN and AlN

V. Yu. Davydov,* Yu. E. Kitaev, I. N. Goncharuk, and A. N. Smirnov
Ioffe Physical Technical Institute, St. Petersburg 194021, Russia

J. Graul, O. Semchinova, and D. Uffmann
LFI Universitat Hannover, Schneiderberg 32, 30167 Hannover, Germany

M. B. Smirnov and A. P. Mirgorodsky
Institute for Silicate Chemistry, St. Petersburg 199155, Russia

R. A. Evarestov
St. Petersburg State University, St. Petersburg 199034, Russia
(Received 4 March 1998; revised manuscript received 1 June 1998)

We present the results of room- and low-temperature measurements of second-order Raman scattering for perfect GaN and AlN crystals as well as the Raman-scattering data for strongly disordered samples. A complete group-theory analysis of phonon symmetry throughout the Brillouin zone and symmetry behavior of phonon branches, including the analysis of critical points, has been performed. The combined treatment of these results and the lattice dynamical calculations based on the phenomenological interatomic potential model allowed us to obtain the reliable data on the phonon dispersion curves and phonon density-of-states functions in bulk GaN and AlN. [S0163-1829(98)06840-4]

I. INTRODUCTION

Group III-V nitride semiconductors GaN, AlN, and their solid solutions are highly attractive materials because of their great potential for development of optoelectronic devices in short-wave length optoelectronics and high-temperature electronics. In spite of remarkable progress in the growth of GaN and related group-III nitrides and in the fabrication technologies of the devices using these materials,[1] some basic properties of GaN and AlN (and among them phonon dispersion) still remain poorly studied. The phonon spectrum is one of the fundamental characteristics of crystals. The behavior of phonon dispersion branches reflects specific features of the crystal structure and the interatomic interactions and, therefore, gives the most comprehensive and detailed information about the dynamical properties of crystals. The phonon dispersion curves are typically obtained by the neutron-scattering technique. However, the absence of GaN and AlN crystals of sufficiently large sizes makes neutron measurements difficult.

Several attempts have been made to calculate the phonon spectra for GaN and AlN. The phenomenological model treatments for hexagonal GaN and AlN have been reported in Refs. 2–4, whereas the *ab initio* calculations for these crystals have been made in Refs. 5 and 6. However, the phenomenological calculations of phonon dispersion curves and the phonon density-of-states (DOS) function in Ref. 4 were actually performed only for hexagonal AlN whereas for the hexagonal GaN the assumption of similarity between GaN and AlN has been proposed. The *ab initio* calculations of phonon dispersion curves are available only for hexagonal AlN (Ref. 5), however, the data on the phonon DOS function are not given there. Finally, it should be noted that the symmetry assignment of phonon dispersion curves at the Brillouin zone (BZ) points other than $k=0$ as well as their symmetry behavior throughout the BZ (including ''crossing'' and ''anticrossing'' effects) have not yet been reported in the literature.

The phonon dispersion curves can also be extracted from the experimental data. However, as noted above, the most direct neutron-scattering technique cannot be used for these crystals. A less direct, but potentially very accurate method for probing the phonons with nonzero wave vectors involves the analysis of the second-order Raman spectra. Second-order Raman scattering is a high-order scattering process, and all of the phonons throughout the BZ can be Raman active. It is known that the features of the two-phonon spectra are determined by the peculiarities in the phonon DOS function closely associated with the flat regions of the phonon dispersion curves. It is also possible to obtain information on the phonon DOS function from the Raman spectrum of the sample having a strongly disordered crystalline lattice. The efficiency of this approach has been demonstrated for amorphous silicon and other materials.[7]

As far as we know, no data on the second-order Raman scattering in AlN have been published, and there is only one work where an attempt was made to compare the second-order GaN spectrum with the calculated phonon dispersion curves.[3] There are no Raman data to our knowledge, for amorphous GaN and AlN or for GaN and AlN with a strongly disordered crystalline structure (for instance, as a result of ion implantation) as well.

The goals of our studies were (i) to obtain detailed experimental information on the phonon spectra of hexagonal GaN and AlN at room and cryogenic temperatures by Raman scattering; (ii) to perform a complete group-theory analysis of phonon symmetry throughout the BZ; and (iii) to calculate the phonon dispersion curves and DOS functions for GaN

TABLE I. Potential function parameters of wurtzite GaN and AlN.

	Ionic charge (e)	Force constants (mdyn/A)					
	Z	B	A_r (M-N_1)	A_r (M-N_2)	A_r (M-M)	A_r (N-N)	A_α (N-M-N) A_α (M-N-M)
GaN	1.14	−0.17	1.89	1.89	0.10	0.10	0.20
AlN	1.25	−0.22	2.43	2.18	0.20	0.10	0.16

and AlN taking into account the experimental Raman-scattering data and the results of the analysis of the symmetry behavior of phonon branches.

II. EXPERIMENT

All of the samples studied were grown on the (0001) α-Al_2O_3 substrates. The GaN samples were approximately 1-μm-thick layers grown by molecular-beam epitaxy (MBE) and the 50–70–μm-thick layers prepared by chloride-hydride–vapor-phase epitaxy (CHVPE). A typical carrier concentration in the layers was of the order of 1×10^{17} cm^{-3}. In special cases the samples with a high carrier concentration of about 3×10^{19} cm^{-3} were investigated. The AlN samples were initially undoped 5–7-μm-thick layers grown by CHVPE. In order to obtain the disorder-induced Raman scattering, Er ions (energy, $E=1$ MeV; dose, $F=5\times10^{14}$–5×10^{15} ion/cm^2) were implanted into these samples.

The Raman spectra of the GaN and AlN layers were measured at temperatures ranging from 6.0 to 300 K using a double grating monochromator and an Ar^+ laser ($\lambda=488$ nm) as a source of excitation. Both the backscattering and the 90° scattering geometries were used. Some experiments were carried out using a microscopic attachment that allowed us to record information when the incident beam hit the edge of the GaN or AlN layer. A Ne lamp was used to precisely calibrate the monochromator. The accuracy of measured phonon frequencies was about 0.2 cm^{-1}.

III. RESULTS AND DISCUSSION

A. Lattice dynamics model

To simulate the lattice dynamics of the GaN and AlN crystals, a simple phenomenological model based on the short-range interatomic potentials and rigid-ion Coulomb interactions has been developed. In the model, the Coulomb interactions are described by the rigid ion model (RIM) using the only value, i.e., ionic charge Z. The short-range force field includes metal-nitrogen (M-N), metal-metal (M-M), and nitrogen-nitrogen (N-N) pairwise bond stretching force constants $[A_r=(d^2\varphi/dr^2)]$ complemented by the M-N-M and N-M-N bending force constants $[A_\alpha=(1/r^2)\times(d^2\varphi/d\alpha^2)]$. No nondiagonal parameters were used. There are two nonequivalent M-N distances in the wurtzite structure. Thus we used two different M-N stretching force constants: the first one (M-N_1) was perpendicular to the c axis and the second one (M-N_2) was parallel to it. In order to satisfy the static equilibrium condition, the first derivatives of the short-range M-N potentials were considered, and the parameter $B=(1/r)(d\varphi/dr)$ (taken to be equal for M-N_1 and M-N_2 bonds) was involved in the calculations.

Thus the model corresponds to the mixed ionic-covalent nature of chemical binding. The values of the model parameters were evaluated by fitting the available experimental data (with the exception of the B parameter determined from the equilibrium condition). However, our calculations have revealed that the inclusion of the upper B_1 silent mode frequency in the fitting procedure can considerably influence the net result. This mode cannot be observed in the Raman or infrared (IR) measurements, but its *ab initio* frequency estimations are available in the literature.[5,6] These values of the B_1 mode frequencies were used along with the experimental data (optically active mode frequencies and elastic constants) involved in the fitting procedure for hexagonal AlN and GaN. The model parameters are listed in Table I and the results of fitting thus obtained are given in Tables II and III.

In general, our approach is close to that used in Refs. 3 and 4. However, the following features of the present model

TABLE II. Zone-center phonon frequencies (cm^{-1}) of hexagonal GaN and AlN.

Mode	GaN					AlN				
	Calc. this work	Expt. this work		*ab initio* Ref. 6	Expt. Ref. 17	Calc. this work	Expt. this work		*ab initio* Refs. 5, 21	Expt. Ref. 20
		$T=300$ K	$T=6$ K				$T=300$ K	$T=6$ K		
E_2 (low)	153	144.0	143.6	143	144	252	248.6	248.4	237	252
B_1 (low)	319			337		571			580[a]	
A_1 (TO)	546	531.8	533.8	541	533	615	611.0	613.8	619	614
E_1 (TO)	554	558.8	560.2	568	561	673	670.8	673.4	677	673
E_2 (high)	565	567.6	569.0	579	569	667	657.4	660.0	667	660
B_1 (high)	728			720		778			765[a]	
A_1 (LO)	734	734.0	736.6	748	735	881	890.0	894.0	893	893
E_1 (LO)	739	741.0	744.0	757	743	922	912.0	917.0	919	916

[a]Estimated from dispersion curves given in Ref. 5.

TABLE III. Elastic constants (GPa) of hexagonal AlN and GaN.

	GaN			AlN		
El. const.	This work	Ref. 26	Ref. 25	This work	Ref. 24	Ref. 20
C_{11}	315	390	296	419	345	411
C_{12}	118	145	120	177	125	149
C_{13}	96	106	158	140	120	99
C_{33}	324	398	267	392	395	389
C_{44}	88	105	24	110	118	125
C_{66}	99	123	88	121	110	131

distinguish it from the preceding works. (i) The bend-bend interaction is omitted. (ii) The A_α (M-N-M) values are positive. Note that the negative bending force constant can hardly be physically justified. According to our estimates, the negative bending force constants would provide the elastic properties inconsistent with the measured ones. (iii) The condition that a shorter bond should be harder is satisfied. (iv) The lattice under consideration is strain free (the electrostatic compression forces are balanced by the bond tensions).

By using the obtained parameter set, the phonon spectra for the entire BZ and the phonon DOS function were calculated within the standard schemes of the lattice dynamics[8] by using the CRYME program.[9] To calculate the phonon DOS function, the BZ was divided into $24\times24\times24$ meshes, and the symmetry was taken into account to reduce the number of independent wave vectors. As a result, we obtained the phonon dispersion curves and DOS functions for GaN and AlN shown in Figs. 1 and 2, respectively.

B. Group-theory analysis

The symmetry of phonons in the hexagonal GaN and AlN crystals was determined using the method of induced band representations of space groups.[10] This method allows one to connect by symmetry the local atomic displacements of particular atoms in the primitive cell and normal modes throughout the BZ. GaN and AlN with the wurtzite structure belong to the space group C_{6v}^4 ($P6_3mc$) with two formula units per primitive cell. Both Ga(Al) and N atoms occupy $2b$ sites of symmetry C_{3v}. The results of the group-theory analysis are presented in Table IV.

In Table IV, column 1 contains atoms occupying the Wyckoff position **q** given in column 2 together with its coordinates and site symmetry group. Columns 4–6 contain indices of small irreducible representations (irreps) induced by those irreps β (column 3) of the site symmetry group according to which the local atomic displacements (x,y,z) are transformed. (The small irreps are labeled according to Ref. 11.) The induced representations determine symmetries of phonons at the symmetry points of the BZ, which are given together with their coordinates and little groups in the headings of columns 4–6. The sets of normal modes at the symmetry points of the BZ are obtained by summing up contributions of all the atoms in the primitive cell. As a result, we have

$$\Gamma \text{ point: } \Gamma_{ac}+\Gamma_{opt}=2(\Gamma_1+\Gamma_4+\Gamma_5+\Gamma_6)$$
$$=2(A_1+B_1+E_1+E_2),$$
$$\Gamma_{ac}=\Gamma_1+\Gamma_6=A_1+E_1;$$
$$\Gamma_{opt}=\Gamma_1+2\Gamma_4+2\Gamma_5+\Gamma_6=A_1+2B_1+2E_2+E_1$$
$$K \text{ point: } 2(K_1+K_2+2K_3);$$
$$M \text{ point: } 2(2M_1+M_2+M_3+2M_4). \quad (1)$$

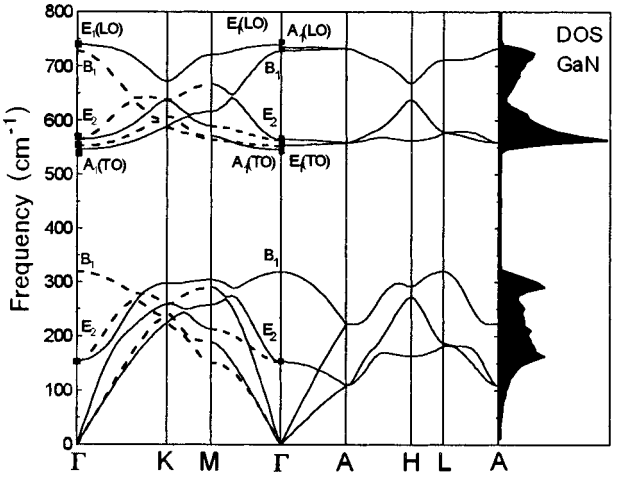

FIG. 1. Calculated phonon dispersion curves for bulk GaN. The solid and dashed lines correspond to the Λ_1 (or T_1) and Λ_2 (or T_2) irreps, respectively.

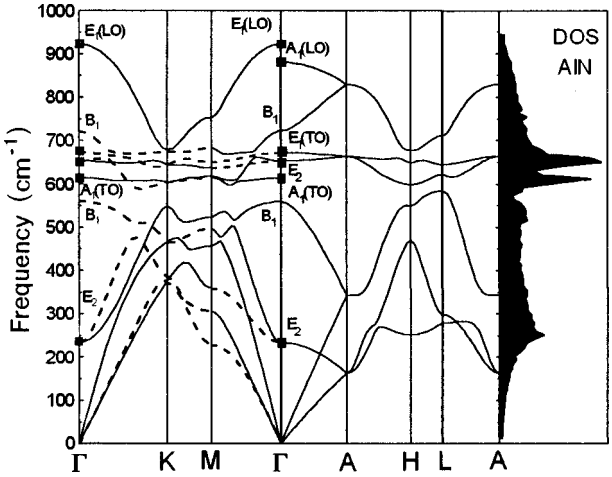

FIG. 2. Calculated phonon dispersion curves for bulk AlN. The solid and dashed lines correspond to the Λ_1 (or T_1) and Λ_2 (or T_2) irreps, respectively.

TABLE IV. Phonon symmetry in hexagonal GaN and AlN.

Atom	**q**	β	Γ (000) C_{6v}	K ($\frac{1}{3}\frac{1}{3}0$) C_{3v}	M ($\frac{1}{2}00$) C_{2v}
Ga(Al)	$2b$	$a_1(z)$	1,4	3	1,4
N	$(\frac{1}{3}\frac{2}{3}z)$ $(\frac{2}{3}\frac{1}{3}z+\frac{1}{2})$ C_{3v}	$e(x,y)$	5,6	1,2,3	1,2,3,4

At the Γ point, the correspondence between the two common notations of irreps is the following: $\Gamma_1=A_1$, $\Gamma_4=B_1$, $\Gamma_5=E_2$, $\Gamma_6=E_1$.

To obtain the phonon symmetry, it is sufficient to analyze the points of the K set only. The phonon symmetry at other points in the BZ can be obtained from the compatibility relations. It should be pointed out that different space groups having the same Bravais lattice can have different K sets in the BZ. For the hexagonal lattice, the K set in the holohedric space groups (with the highest point symmetry D_{6h}) consists of Γ, A, K, H, M, and L points, which are isolated symmetry points, whereas for the C_{6v}^4 group the points A, H, and L become points at symmetry lines. As a result, the K set reduces to the Γ, K, and M points, which are the points at the intersection of the $k_z=0$ plane with these symmetry lines. Knowing the phonon symmetry at the Γ, K, and M points, we can easily write the sets of normal modes at the A, H, and L points using the compatibility relations. Hence,

$$A \text{ point: } 2(A_1+A_4+A_5+A_6),$$

$$H \text{ point: } 2(H_1+H_2+2H_3),$$

$$L \text{ point: } 2(2L_1+L_2+L_3+2L_4), \tag{2}$$

taking into account that most of the irreps at these points become complex conjugate and form coreps A_1+A_4, A_5+A_6, H_1+H_2, L_1+L_4, and L_2+L_3 describing the degenerate phonon states. This degeneracy is connected with the time inversion and can be lifted, e.g., by applying an external field.

We can see from Table IV that, from the point of view of symmetry both atoms, Ga(Al) and N, contribute equally to all the modes. In this case the z displacements of both atoms contribute to the Γ_1 and Γ_4 modes, whereas the x, y displacements contribute to Γ_5 and Γ_6.

From Table IV, one can also establish the symmetry behavior of particular phonon branches induced by particular atomic displacements. Note that by using the compatibility relations it is impossible to establish the one-to-one symmetry correspondence between the irreps of Γ and K (Γ and M) points. Nevertheless, in Ref. 3 the following correspondence between the modes: Γ_1-K_1, Γ_4-K_2, Γ_5-K_3, and Γ_6-K_3 was suggested. However, the results of our analysis show, e.g., that the symmetry behavior of phonon branches induced by z displacements is as follows: (Γ_1,Γ_4)-K_3-(M_1,M_4). This means that two doubly degenerate K_3 modes split in the Γ-K and K-M directions transforming into two pairs of Γ_1 and Γ_4 modes and two pairs of M_1 and M_4 modes, respectively. For the phonon branches induced by the x,y displacements, one can see the $\Gamma_5+\Gamma_6$ modes transform into the $K_1+K_2+K_3$ modes, which in turn transform into the $M_1+M_2+M_3+M_4$ modes. The picture becomes more complicated when phonon branches intersect. It should be noted that when comparing our results with those in Ref. 3, one should keep in mind that we follow the labeling of irreps of Ref. 11, which differ from the notation used in Ref. 3. In particular, the irreps labeled as Γ_4, A_4, Γ_5, A_5, Γ_6, and A_6 in our case correspond, respectively, to Γ_3, A_3, Γ_6, A_6, Γ_5, and A_5 in Ref. 3.

In the first-order optical spectra, the A_1 (z;xx,yy,zz) and E_1 (x,y;xz,yz) optical modes are both Raman and IR active and both the longitudinal (LO) and transverse (TO) components can be observed in the Raman spectra. The two E_2 (xx,yy,xy) modes are only Raman active and the two B_1 modes are silent modes. The overtones and combinations of phonons in the second-order Raman and infrared optical spectra obey the selection rules given in Ref. 3.

There is another restriction imposed on the phonon symmetry for the phonons to be seen in the second-order Raman spectra. The phonons should correspond to the extremums of the phonon DOS function that are related to the flat regions (i.e., the zero-slope or critical points) of phonon dispersion curves. The equation $\nabla_{\mathbf{k}}\omega(\mathbf{k_0})=0$ defining the critical points $\mathbf{k_0}$ can be a result of symmetry (symmetry critical points) or follow from a particular form of the interatomic interaction potential (singular critical points). The symmetry critical points are determined by the interaction potential symmetry alone and are not affected by variations in the potential parameters. These points can be obtained using the procedure described in Refs. 10, 12, and 13. In the procedure one should distinguish two cases: (i) Wave vectors $\mathbf{k_0}$ and $-\mathbf{k_0}$ do not belong to the same wave-vector star (this case is not realized in the space group C_{6v}^4). (ii) Wave vectors $\mathbf{k_0}$ and $-\mathbf{k_0}$ belong to the same wave-vector star (Γ, A, M, L, K, and H points for the space group C_{6v}^4). In this case, for a $\mathbf{k_0}$ point to be a symmetry critical point for a particular phonon dispersion curve $\omega_j(\mathbf{k_0})$ described by a small irreducible corepresentation $(\mathbf{k_0},j)$, the following relation should be satisfied:

$$\sum \chi^v(h)|\chi^{\mathbf{k}\mathbf{0}\cdot j}(g)|^2-\chi^v(h_0h)|\chi^{\mathbf{k}\mathbf{0}\cdot j}(g_0gg_0g)|^2=0,$$

$$h\in G_{\mathbf{k_0}} \tag{3}$$

where $\chi^{\mathbf{k}\mathbf{0}\cdot j}(g)$ and $\chi^v(h)$ are the characters of small irreducible corepresentation $(\mathbf{k_0},j)$ and the vector representation of the little group $G_{\mathbf{k_0}}$, respectively, and $g_0=(h_0|\mathbf{a_0})$ is any element with the property $h_0\mathbf{k_0}=-\mathbf{k_0}+\mathbf{b}$. In turn, this case

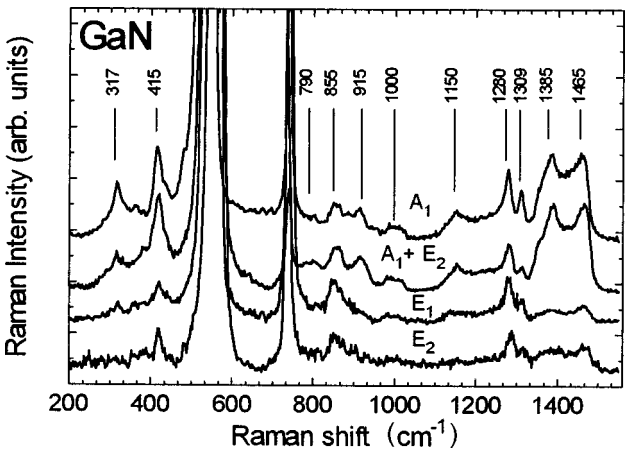

FIG. 3. Second-order Raman spectra for GaN taken at room temperature for various scattering geometries corresponding to the A_1, A_1+E_2, E_1, and E_2 symmetries.

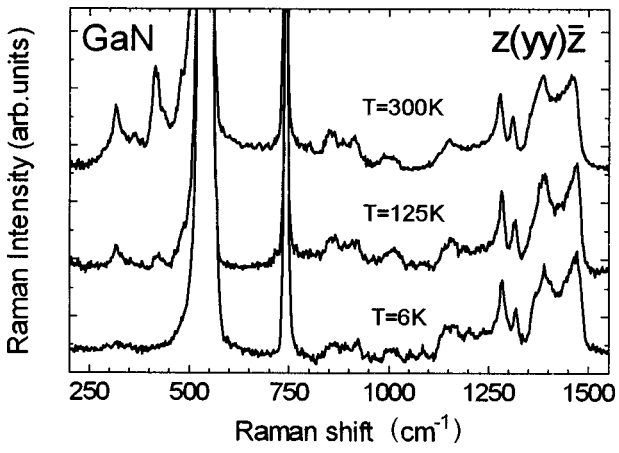

FIG. 4. Polarized second-order Raman spectrum obtained at different temperatures for the GaN layer.

can be subdivided into two subcases: (a) Wave vectors $\mathbf{k_0}$ and $-\mathbf{k_0}$ are equivalent, i.e., $\mathbf{k_0}=-\mathbf{k_0}+\mathbf{b}$ (Γ, A, M, and L points for the space group C_{6v}^4). (b) Wave vectors $\mathbf{k_0}$ and $-\mathbf{k_0}$ are not equivalent, i.e., $\mathbf{k_0}\neq-\mathbf{k_0}+\mathbf{b}$ (K and H points for the space group C_{6v}^4).

The symmetry analysis using Eq. (3) shows that only the Γ and M points are symmetry critical points for all the phonon branches, whereas the zero slopes of the calculated phonon dispersion curves $\omega(\mathbf{k})$ at other points of the BZ (at K and H, see Figs. 1 and 2) result from a particular form of the interaction potential, i.e., the K and H points are singular critical points.

C. Raman spectra of hexagonal GaN and AlN

We have thoroughly studied the polarized first-order Raman spectra of GaN and AlN at room and cryogenic temperatures. The Raman spectra of these materials have recently been studied in Refs. 14–20. On the whole, our results are consistent with the results of these works. The most important finding of our study is that all six Raman-active modes, i.e., $1A_1(\mathrm{TO})+1A_1(\mathrm{LO})+1E_1(\mathrm{TO})+1E_1(\mathrm{LO})+2E_2$, are observed in the spectra of GaN and AlN. The polarization measurements of these spectra have revealed an excellent agreement with the selection rules given in Ref. 22. Thus, the obtained Raman data clearly demonstrate that the samples under study can be characterized as high-quality epitaxial layers of hexagonal GaN and AlN. This conclusion is fully consistent with the x-ray data. The half-widths of the rocking curves at the (0002) reflection measured in the (ω) scanning geometry were 130–150 arc sec. The Γ-point phonon frequencies obtained in this work for strain-free GaN and AlN layers at room and helium temperatures are summarized in Table II.

We have also studied the polarized second-order Raman spectra for GaN and AlN and made an assignment of spectral features using the Raman selection rules and calculated dispersion curves. In addition, a thorough analysis of the temperature dependence of the second-order Raman spectra was performed. The frequencies of the main features observed in the polarized second-order Raman spectra of GaN (see Fig. 3), together with their assignments to definite phonon branches, are consistent, in general, with those of Ref. 3. However, there is a significant distinction. According to Ref. 3, the doublet structure observed at 410 and 420 cm^{-1} can be attributed to the *overtones* of transverse acoustic phonons at the symmetry points A (or K) and M, respectively. In contrast to Ref. 3, we could not detect the actual doublet structure. The temperature dependence of the asymmetric feature near 415 cm^{-1} (see Fig. 4) argues for its assignment to a *difference combination* of optical and acoustic phonons. This is also confirmed by the presence of a pronounced peak near 415 cm^{-1} in the difference DOS function obtained from our calculations. The analysis based on the group-theoretical selection rules allows us to assign this peculiarity to the combination of optical and acoustic branches at the M point.

Figure 5 shows the polarized second-order Raman spectra of the AlN sample obtained at room temperature. Using the selection rules in combination with the phonon dispersion curves $\omega(\mathbf{k})$, we tried to assign the features in the second-order Raman spectra to the phonons of definite types of symmetry. There were several factors that made this task rather complicated. First, the spectral region corresponding to the overtones and combinations of acoustic phonons also included intense first-order Raman lines that made the interpretation of this region very difficult. Second, the second-order

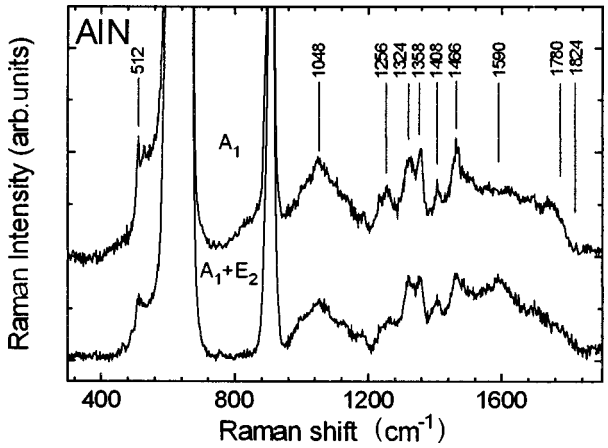

FIG. 5. Second-order Raman spectra for AlN taken at room temperature for scattering geometries corresponding to the A_1 and A_1+E_2 symmetries.

TABLE V. Frequencies (cm^{-1}), symmetries and assignments of strongest modes in the second-order Raman spectra of hexagonal AlN.

Frequency cm^{-1}	Symmetry	Process	Point
512	$A_1,(E_2)$	Acoust. overtone	
611	A_1	First order, A_1 (TO)	Γ
657	E_2	First order, E_2 (high)	Γ
670	E_1	First order, E_1 (TO)	Γ
890	A_1	First order, A_1 (LO)	Γ
912	E_1	First order, E_1 (LO)	Γ
1048	A_1,E_2	Acoust, overtone and acoust.-opt. comb.	
1256	$A_1,(E_2)$	Optic. overtone, $[K_3,M]^2$	*K,M*
1324	A_1	Optic. comb. and optic. overtone	
1358	$A_1,(E_2)$	Optic. overtone	
1408	A_1	Optic. comb.	
1466	A_1,E_2	Optic. comb., $M_i \times M_i$	*M*
1500	A_1	Optic. overtone., $[K_i]^2$	*K*
1590	A_1,E_2	Optic. overtone, $[M_i]^2$	*M*
Cutoff 1824	A_1,E_2	Optic. overtone, $[E_1\ (\mathrm{LO})]^2$	Γ

Raman spectrum corresponding to combinations of the acoustic and optical phonons was a broad band with a poorly defined structure. The low-temperature studies of this spectral region have not revealed any structure either. Third, it was difficult to obtain the polarized spectra because of a very low intensity of the second-order Raman spectra. For this reason, only the spectra corresponding to the polarizations in which A_1 and A_1+E_2 phonons are Raman active were reliably detected at room and low temperatures in the spectral region where the second-order processes resulting from scattering of optical phonons dominate and that has a well-defined structure. Thus the results given in Table V for AlN should be regarded as tentative at this stage of research.

D. Discussion

In the framework of the developed phenomenological model (Sec. III A), we calculated the phonon dispersion curves and DOS functions for GaN and AlN using the experimental frequencies of the zone-centered phonons and the phonons at the BZ boundaries and the group-theory information on the symmetry behavior of phonon branches throughout the BZ (Sec. III B). In turn, the phonon frequencies at the BZ boundary were estimated from the second-order Raman spectra using the results of the group-theory analysis as well as the dispersion curves calculated at the previous approximation step. So this is a self-consistent procedure.

Let us begin with the results for AlN. We have compared the obtained dispersion curves with the ones derived from the *ab initio* calculations of Ref. 5. No important differences between our results and the *ab initio* calculations were found for the high-frequency dispersion branches. However, the situation was different for the low-frequency phonon branches along the Γ-(Λ)-*K*-(T)-*M* line near the *K* point (see Fig. 2). Our calculations have shown that along this line the LA branch originating from the Γ_1 (A_1) mode and the lower branch originating from the Γ_5 (E_2) optical mode belong to the same Λ_1 (or T_1) irrep. Due to this, they interact and mutually repulse, thus manifesting an anticrossing effect. As a consequence, on approaching the *K* point, the K_1 modes belonging to the Γ_5-K_1 branch have higher frequencies than the K_3 modes of the LA branch (Γ_1-K_3). These results are consistent with our group-theory predictions. It should be noted that we performed our calculations by explicitly using the symmetry factorization of the dynamic matrix. Therefore, we were able to distinguish the branches with different symmetries and thus to resolve rigorously the problem of their crossing. The anticrossing effect mentioned above was not discovered in Ref. 5 where the phonon branch symmetry was not considered.

We have also compared the calculated phonon DOS function with the experimental results using the disorder-induced Raman spectrum. Such an approach is justified since all the phonons are allowed to participate in the light scattering from the disordered structure. In this case, the Raman spectrum should display the entire phonon DOS function weighted by the transition matrix elements involved in the photon-phonon coupling during the scattering process. In our experiments Er-implanted AlN samples (energy of ions, $E=1$ MeV; dose 5×10^{15} ion/cm^2) were studied. The dose for implantation was chosen so that no intense peaks corresponding to the zone-center phonons were detected in Raman measurements. The spectra were recorded at $T=6$ K to exclude the phonon occupation number. The low-temperature Raman spectrum of Er-implanted AlN is shown in Fig. 6 (curve *c*). To our knowledge, there is only one work reporting the experimental data on the DOS function of AlN that were obtained in the low-temperature neutron studies of AlN fine powder.[23] For comparison, Fig. 6 shows the phonon DOS function (curve *e*) taken from Ref. 23. It can be seen that curves *c* and *e* are in an excellent agreement. Therefore, the Raman spectrum induced by defects in Er-implanted AlN sample reveals all the peculiarities of the phonon DOS function in the regions of both optical and acoustic phonons. Figure 6 also presents the calculated one-phonon DOS function for AlN (curve *d*). A good correspondence between the calculated phonon DOS function, the disorder-induced Raman spectrum of Er-implanted AlN, and the experimental phonon DOS function obtained from the neutron data favors our model results.

Figure 6 also depicts the low-temperature second-order spectrum with scaling the frequency axis by a factor of $\frac{1}{2}$ (the overtone approximation). It can be seen that the basic features of this spectrum correlate well with the features of the neutron-weighted phonon DOS function. Thus the second-order spectra can indeed be used as a test for model calculations (see Table V).

Now we turn to GaN. As noted above, the *ab initio* calculations of phonon dispersion branches for hexagonal GaN are not available. The model calculations of phonon dispersion branches for GaN were performed in Refs. 3 and 4. In general, our dispersion curves for GaN agree well with the data given in these works for the low-frequency region (<400 cm^{-1}). However, just like for AlN, they differ along the Γ-(Λ)-*K*-(T)-*M* line near the *K* point where the anticrossing effects are essential (see Fig. 1). Moreover, the behavior of the high-frequency optical phonons markedly dif-

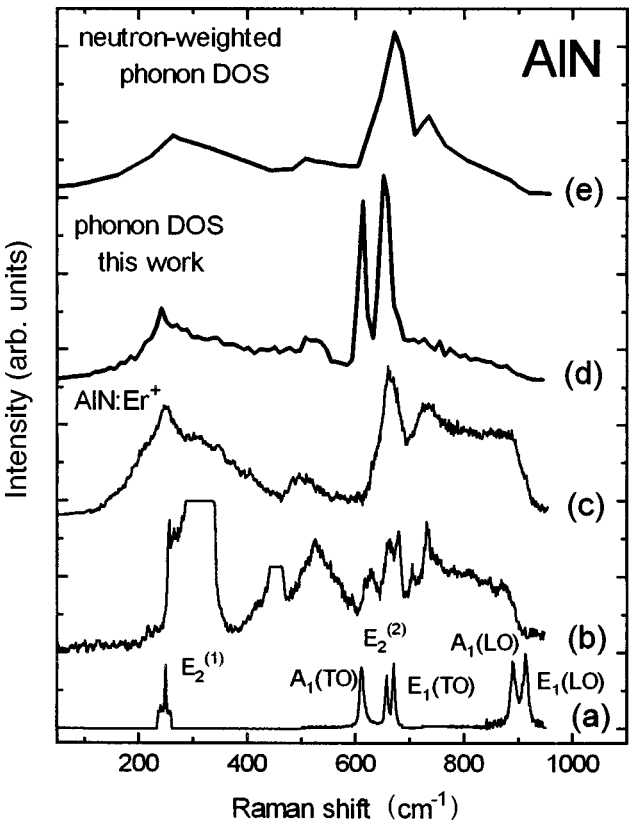

FIG. 6. (a) First-order Raman spectrum of the AlN sample, (b) second-order Raman spectrum of the AlN sample with scaling the frequency axis by a factor of $\frac{1}{2}$, (c) Raman spectrum of the Er-implanted AlN, (d) calculated phonon DOS function for AlN, and (e) neutron-weighted phonon DOS function for AlN fine powder taken from Ref. 23.

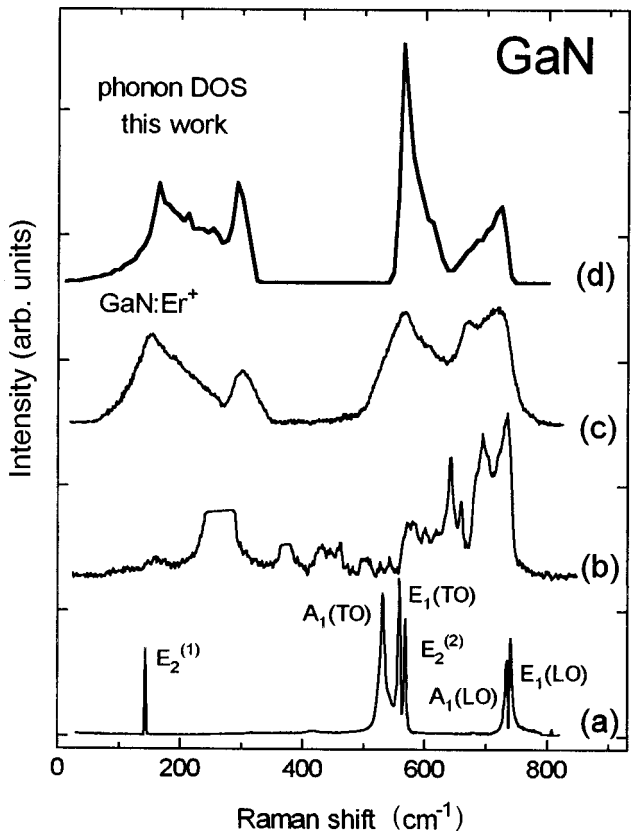

FIG. 7. (a) First-order Raman spectrum of the GaN sample, (b) second-order Raman spectrum of GaN sample with scaling the frequency axis by a factor of $\frac{1}{2}$, (c) Raman spectrum of the Er-implanted GaN, and (d) the calculated phonon DOS function for GaN.

fers from that reported in Refs. 3 and 4. To our belief, the main reason for this is the value of the upper B_1-mode frequency which was taken in our calculations in accordance with the recent *ab initio* results and that is close to the LO (Γ_1) mode frequency.[6] As a result, our model predicts the flatness of the high-frequency phonon branches in GaN. In contrast, in Refs. 3 and 4 the position of the B_1 mode was taken to be much lower than the position of the LO (Γ_1) mode, similar to the situation for AlN. As a result, the authors obtained similar behaviors of the phonon dispersion curves of GaN and AlN.

Assuming that the disorder-induced Raman spectrum can also be used to check the correctness of the model calculations for GaN, we investigated Er-implanted GaN samples. Note that in this case lower implantation doses were sufficient because even for the dose of 1×10^{15} ion/cm^2 the Raman spectra of implanted samples did not exhibit the zone-center phonon lines. The low-temperature Raman spectrum of Er-implanted GaN (curve *c*) and the calculated phonon DOS function (curve *d*) are shown in Fig. 7. The major features of the calculated phonon DOS function and disorder-induced Raman spectrum are seen to correlate well in the entire spectral region, thus confirming the validity of our model calculations.

Figure 7 also presents the low-temperature second-order Raman spectrum with scaling the frequency axis by a factor of $\frac{1}{2}$ (curve *b*). Its highest-frequency part in the form of two peaks at 1385 and 1465 cm^{-1} is seen to correlate with the region of dispersion of the LO phonons (see Fig. 1). According to our measurements and the data from Ref. 3, the peak near 1385 cm^{-1} is due to the scattering processes originating from the K point of the BZ. The position of the peak near 1465 cm^{-1} corresponds to that of the overtone of the zone-center A_1 (LO) mode. However, as follows from our calculations (see Fig. 1), the upper optical branches are rather flat, thus providing a strong peak in the phonon DOS function close to the LO (Γ) position. It can be supposed that this will lead to a peculiarity in the second-order spectrum at the frequency close to the overtone of the zone-center A_1 (LO) mode. In order to clarify the situation, we studied samples with different carrier concentrations on the assumption that screening of the LO modes by carriers will manifest itself in the second-order spectra.

Figure 8 shows the Raman spectra in the frequency region of interest for two samples. Spectrum 1 in Fig. 8 is obtained for the sample with a low concentration of free carriers (of the order of 1×10^{17} cm^{-3}), which is evidenced by the presence of a well-formed LO phonon near 735 cm^{-1}. Spectrum 2 in Fig. 8 is obtained for the sample with a high concentration of free carriers (of the order of 3×10^{19} cm^{-3}) as demonstrated by the absence of the LO-phonon mode. As can be seen from the second-order Raman spectra for these two samples, the low-frequency parts in the camelbacklike structure lying between 1340 and 1495 cm^{-1} fully coincide, whereas the high-frequency parts markedly differ. Thus the

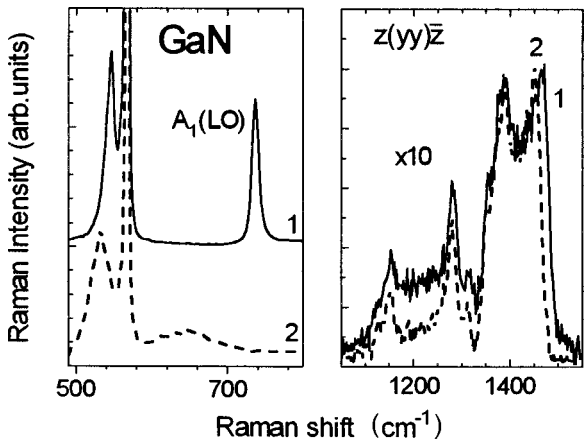

FIG. 8. Polarized second-order Raman spectra for the GaN layers with different carrier concentrations ($1-n=1\times10^{17}$ cm^{-3}, $2-n=3\times10^{19}$ cm^{-3}).

obtained data indicate that only the high-frequency part of the peak near 1465 cm^{-1} indeed corresponds to the overtone of the zone-center A_1 (LO) mode. The remaining part of the peak appears to be due to the flat character of upper optical branches.

Thus the whole body of the experimental and theoretical evidence points to substantially different behaviors of high-frequency optical branches in hexagonal GaN and AlN. In contrast to phonon dispersion in AlN, high-frequency branches in GaN are flat for most of the BZ, thus creating a high-frequency peak in the phonon DOS function. In our opinion, the ''immobility'' of the heavy Ga sublattice is responsible for the above effect. Indeed, the heavy Ga atoms remain nearly motionless for the high-frequency modes in GaN. As a result, the N atoms vibrate in the isotropic field of the intratetrahedral forces and, therefore, the relevant frequencies are nearly independent of the atomic displacement orientations and of the wave-vector values. This leads to a small dispersion of the optical-phonon branches. This is not the case for the high-frequency vibrations of the AlN sublattice in which the contributions of Al atoms are significant. Consequently, the LO branches display a large dispersion throughout the BZ that accounts for the absence of peaks in the high-frequency part of the phonon DOS curve.[27–29]

The flatness of the optical-phonon branches in cubic GaN was also revealed in a recent *ab initio* study.[30] As a result, the phonon DOS functions for cubic AlN (Ref. 31) and cubic GaN were found to be very different in the high-frequency region. Our results reveal the same difference in the dynamical properties of the wurtzitelike AlN and GaN.

IV. SUMMARY

To summarize, we have carried out detailed studies of the first-order GaN and AlN Raman spectra at room and low temperatures. The second-order Raman spectrum for AlN and the Raman spectra of strongly disordered samples have been obtained. It has been demonstrated that the phonon DOS function can be extracted from the Raman spectra of strongly disordered samples. Using the method of induced band representations of space groups, we have performed a group-theory analysis of the phonon symmetry over the entire BZ and determined which local atomic displacements contribute to them. We have also established the symmetry behavior of particular phonon branches including the analysis of critical points of phonon dispersion curves. The comprehensive approach including three different methods (Raman scattering, lattice dynamical calculations, and group-theory analysis) permitted us to establish the distinguishing features of phonon dispersion curves and DOS functions in GaN and AlN crystals. We have established that the upper optical branches of the hexagonal GaN and AlN crystals exhibit essentially differing behaviors.

ACKNOWLEDGMENTS

The authors would like to thank Professor D. Strauch for giving them the opportunity to become acquainted with the results of his *ab initio* calculations of the phonon dispersion curves and DOS function for cubic AlN before his paper was published. The authors are also grateful to V. P. Smirnov for helpful discussions. J.G., O.S., and D.U. would like to thank Dr. N. Roy, Bonn, and H.-P. Werno, Koblenz, for their support. This work was partly supported by the Russian Foundation for Basic Research (Grant No. 97-02-18088) and the program ''Physics of Solid State Nanostructures'' (Grant No. 97-1035) of the Ministry of Sciences of Russia.

*Electronic address: valery.davydov@pop.ioffe.rssi.ru

[1] S. Nakamura, and G. Fasol, *The Blue Laser Diode, GaN based Light Emitters and Lasers* (Springer-Verlag, Berlin, 1997).

[2] T. Azuhata, T. Matsunaga, K. Shimada, K. Yoshida, T. Sota, K. Suzuki, and S. Nakamura, Physica B **219-220**, 493 (1996).

[3] H. Siegle, G. Kaczmarczyk, L. Filippidis, A. P. Litvinchuk, A. Hoffmann, and C. Thomsen, Phys. Rev. B **55**, 7000 (1997).

[4] C. Gobel, C. Schrepel, U. Scherz, P. Thurian, G. Kaczmarczyk, and A. Hoffmann, in *Proceedings of the International Conference on Defects in Semiconductors-19*, edited by G. Davies and M. H. Nazare [Mater. Sci. Forum **258-263**, 1173 (1997)].

[5] K. Karch and F. Bechstedt, Phys. Rev. B **56**, 7404 (1997).

[6] K. Karch, J.-M. Wagner, and F. Bechstedt, Phys. Rev. B **57**, 7043 (1998).

[7] M. Cardona, in *Light Scattering in Solids II*, edited by M. Cardona and G. Guntherodt, Topics in Applied Physics Vol. 50 (Springer, Berlin, 1982), p. 117.

[8] M. Born and K. Huang, *Dynamical Theory of Crystal Lattices* (Claredon, Oxford, 1988).

[9] M. B. Smirnov, A. P. Mirgorodsky, and P. E. Quintard, J. Mol. Struct. **348**, 159 (1995).

[10] R. A. Evarestov and V. P. Smirnov, *Site Symmetry in Crystals: Theory and Applications*, edited by M. Cardona, Springer Series in Solid State Sciences, Vol. 108 (Springer, Heidelberg, 1993).

[11] S. C. Miller and W. F. Love, *Tables of Irreducible Representations of Space Groups and Corepresentations of Magnetic Space Groups* (Pruett, Boulder, 1967).

[12] O. V. Kovalev, *Representations of the Crystallographic Space Groups*, 2nd ed., edited by H. T. Stokes and D. M. Hatch (Gordon and Breach, New York, 1993).

[13] N. V. Kudryavceva, Fiz. Tverd. Tela (Leningrad) **10**, 1616 (1968) [Sov. Phys. Solid State **10**, 1280 (1968)].

[14] P. Perlin, C. J. Carrilon, J. P. Itie, A. S. Miguel, I. Grzegory, and A. Polian, Phys. Rev. B **45**, 83 (1992).
[15] T. Kozawa, T. Kachi, H. Kano, Y. Taga, M. Hachimoto, N. Koide, and K. Manabe, J. Appl. Phys. **75**, 1098 (1993).
[16] H. Siegle, L. Eckey, A. Hoffman, C. Thomsen, B. K. Meyer, D. Schikora, M. Hankeln, and K. Lischka, Solid State Commun. **96**, 943 (1995).
[17] T. Azuhata, T. Sota, K. Suzuki, and S. Nakamura, J. Phys.: Condens. Matter **7**, L129 (1995).
[18] V. Yu Davydov, N. S. Averkiev, I. N. Goncharuk, D. K. Nelson, I. P. Nikitna, A. S. Polkovnikov, A. N. Smirnov, M. A. Jacobson, and O. K. Semchinova, J. Appl. Phys. **82**, 5097 (1997).
[19] J. A. Sanjurjo, E. Lopez-Cruz, P. Vogl, and M. Cardona, Phys. Rev. B **28**, 4579 (1983).
[20] L. E. McNeil, M. Grimsditch, and R. H. French, J. Am. Ceram. Soc. **76**, 1132 (1993).
[21] L. Filippidis, H. Siegle, A. Hoffman, C. Thomsen, K. Karch, and F. Bechstedt, Phys. Status Solidi B **198**, 621 (1996).
[22] C. A. Arguello, D. L. Rousseau, and S. P. S. Porto, Phys. Rev. **181**, 1351 (1969).
[23] C.-K. Loong, in *Gallium Nitride and Related Materials*, edited by R. D. Dupuis, J. A. Edmond, F. A. Ponce, and S. Nakamura, MRS Symposia Proceedings No. 395 (Materials Research Society, Pittsburgh, 1995), p. 423.
[24] K. Tsubouchi, K. Sugai, and N. Mikoshiba, in *1981 Ultrasonics Symposia Proceedings*, edited by B. R. McAvoy (IEEE, New York, 1981), p. 375.
[25] V. A. Savastenko and A. U. Sheleg, Phys. Status Solidi A **48**, K135 (1978).
[26] A. Polian, M. Grimsditch, and I. Grzegory, J. Appl. Phys. **79**, 3343 (1996).
[27] K. Miwa and A. Fukumoto, Phys. Rev. B **48**, 7897 (1993).
[28] E. Ruiz, S. Alvarez, and P. Alemany, Phys. Rev. B **49**, 7115 (1994).
[29] I. Gorczyca, N. E. Christensen, E. L. Peltzer y Blanca, and C. O. Rodriguez, Phys. Rev. B **51**, 11 936 (1995).
[30] K. Karch, F. Bechstedt, and T. Pletl, Phys. Rev. B **56**, 3560 (1997).
[31] K. Karch, F. Bechstedt, P. Pavone, and D. Strauch, Physica B **219-220**, 445 (1996).